Title

Fluid Flow Measurements in Nanoslits Using Holographic Microscopy

Journal

Langmuir, 41(9)

ISSN

0743-7463

Authors

Yu, Siyang

Orosco, Jeremy

Friend, James

Publication Date

2025-03-11

DOI

10.1021/acs.langmuir.4c04244

Peer reviewed

LANGMUIR

pubs.acs.org/Langmuir
Article

Fluid Flow Measurements in Nanoslits Using Holographic Microscopy

Siyang Yu, Jeremy Orosco, and James Friend*

Cite This: *Langmuir* 2025, 41, 5860−5869
Read Online

ACCESS | Metrics & More | Article Recommendations | Supporting Information

ABSTRACT: To understand the mechanisms driving fluid flow behavior in nanofluidics so that they may be used for on-chip biomedical and chemical applications, the fluid's motion itself needs to be observable and measurable, a difficult challenge at these small scales. We present a new method for measuring both slow and fast flows in nanofluidics using high-speed digital holographic microscopy. We measure the evaporation-driven flow in 25 and 7 nm tall nanoslit channels, showing that the consequent flow speed is about 15 times slower than open atmospheric evaporation due to the confinement of the nanoslit channel. We also measured the surface acoustic wave-driven flow in the 25 nm channel, showing flow at a speed of 0.12 m/s from acoustic wave propagation at 39.7 MHz interacting with the fluid in the channel. A process to eliminate the many sources of noise to produce these results is provided, showing that—in particular—spatial averaging is useful to determine the fluid flow and the dewetting of the fluid in the nanoslit channel over time.

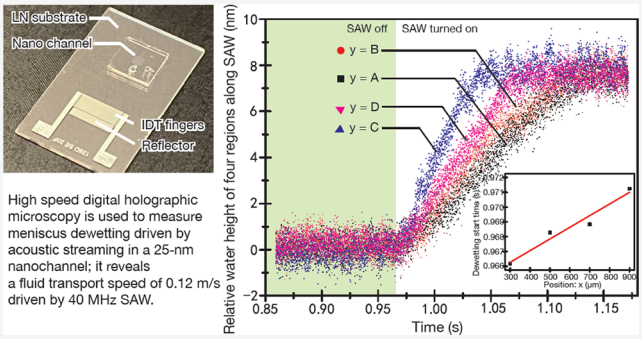

High speed digital holographic microscopy is used to measure meniscus dewetting driven by acoustic streaming in a 25-nm nanochannel; it reveals a fluid transport speed of 0.12 m/s driven by 40 MHz SAW.

INTRODUCTION

Nanofluidic systems offer potentially significant improvements over microfluidics in molecular analysis,[1,2] particularly for biomedical applications.[3−5] They show promise in several other fields, such as enhancing heat transfer, which is beneficial for the operation of integrated circuits.[6−8] Studying nanofluidics is also beneficial because it underpins many cellular mechanisms.[9−11] However, measuring nanoscale fluidic flows, which would be advantageous across these and other disciplines, remains a challenging task.[12−15]

One issue among several in nanofluidics[16,17] is the overwhelming dominance of surface-mediated forces, particularly surface tension-driven[18] capillary forces, over volume-driven forces. The capillary forces at the nanoscale can be extreme: for a w = 10 nm polydimethylsiloxane (PDMS) channel filled with water, the capillary forces, F_{cap}, retaining the water are on the order of 8 MPa (80 atm). For example, taking $\theta = 73°$ as the contact angle of water on a hydrophilic PDMS surface produces $F_{cap} = \frac{4w\lambda_{water}\cos\theta}{w^2} = \frac{4\times10^{-8}\times0.0728}{(10^{-8})^2} = 8.51$ MPa.

Among several methods to manipulate fluids at these scales, acoustic waves are a promising choice, except that they are generally unable to generate large pressures.[13,19] However, through the use of the nonlinear coupling between the acoustic wave propagating in the fluid and the undulating motion of the boundary due to the passage of the acoustic wave, it is possible to generate large pressures in acousto*geometric* streaming[20]—especially in nanoscale channels. So, propulsion of fluids in such small channels may be possible, even with large adverse pressure gradients.

However, imaging the flows in the nanochannels remains extremely difficult. While it is generally straightforward to image the propagation of a fluid meniscus and even the fluid itself in near-nanochannels of 100 nm or greater in height, the imaging of channels at or less than 50 nm is very difficult. There are insufficient changes in the 400 nm or longer wavelengths of visible light passing through such channels to make it possible to "see" what is happening with bright-field imaging, and there is insufficient volume to make fluorescence or luminescence-based imaging practical.[21]

There are many ways to produce images of surfaces and materials all the way to the atomic scale using X-ray, contact, and electron-based imaging methods. These include the nearly routine use of scanning electron and atomic force microscopy methods, as well as scanning tunneling microscopy, scanning ion conductance microscopy (SICM),[22] X-ray diffraction microscopy (XDM),[23] and scanning transmission X-ray microscopy (STXM).[24] Several nanoscale optical imaging methods now exist as well, generally described as super-

Received: October 24, 2024
Revised: February 11, 2025
Accepted: February 12, 2025
Published: February 26, 2025

https://doi.org/10.1021/acs.langmuir.4c04244
Langmuir 2025, 41, 5860−5869

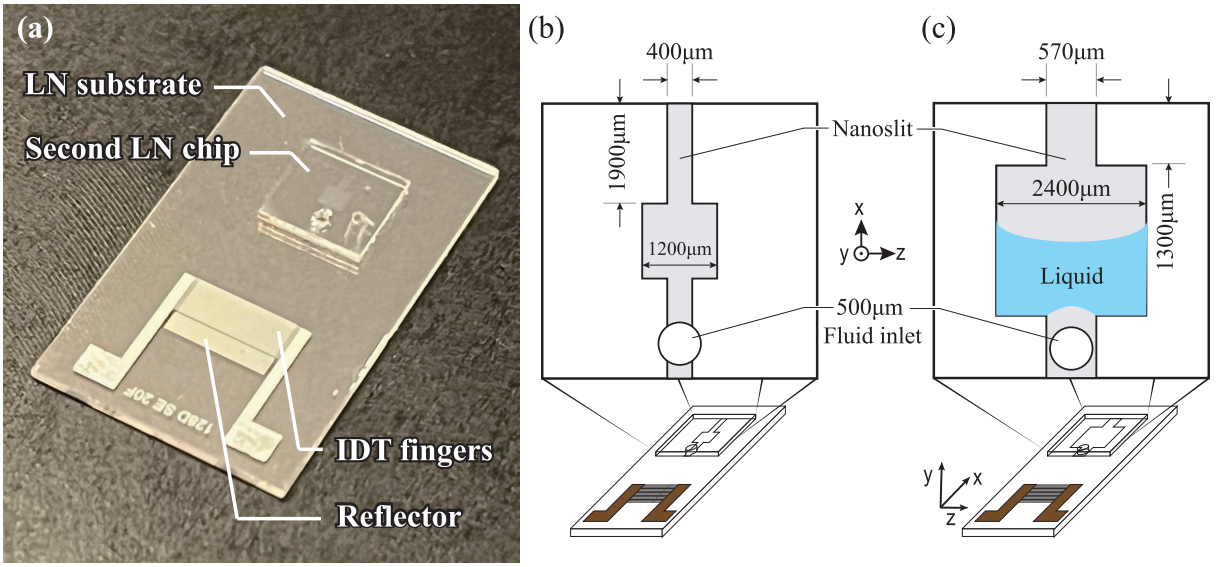

Figure 1. (a) An image of the 25 nm high nanoslit device. The nanoslit between the two LN layers is barely visible. The dimensions of the nanoslit channels and associated fluid inlets for the (b) 25 nm and (c) 7 nm height channels are shown, with a square reservoir present in each design at the center of the 500 μm square second LN chip that is bonded directly onto the LN SAW-carrying substrate. The gap between the second LN chip and the IDT is 5 mm. To prevent the fluid in the fluid inlet from affecting the propagating SAW, it is allowed to evaporate before the experiment is started. The fluid in the nanoslit remains long after the fluid in the fluid inlet evaporates away because the nanoslit channel has much less exposure to the atmosphere.

resolution microscopy.[25] However, all of these methods are unfortunately slow with respect to fluidic phenomena, as they require scanning or fluorophore extinction techniques that take time to produce a complete image. Total internal reflectance microscopy (TIRF) is unique as a potentially fast, visible light imaging method that is also capable of directly resolving nanoscale features. However, it is still subject to the limitations of the wavelength of light and the choice of substrates used in the method.[26]

Here, we introduce a technique for nanofluidic measurement based on high-speed transmission digital holographic microscopy (HSDHM), demonstrating the ability to detect fluid evaporation and fluid transport from acoustogeometric streaming[20] in channels as little as 7 nm in height. The method relies on a change in the propagation time of the light due to changes in the material along its path. The light transmitted through the sample is interfered with light passing around the sample, producing a holograph at the camera plane encoding the geometry of the sample in the field of view. Digital holographic microscopy has been shown in the past to be useful and accurate in imaging fluids[27,28] at the milli and micro scales.[29−33] However, to the authors' knowledge, using digital holographic microscopy to quantify nanoscale fluidic phenomena has not been done, especially using HSDHM to measure rapid fluid phenomena. Imaging such phenomena within channels of 50 nm or less in height is a difficult challenge, as the signal produced from the measurements is often overwhelmed by optical and background noise. Fortunately, with ample spatial and minimal temporal averaging in HSDHM, we show in this work that it is possible to discern nanometer-order changes in the fluid height over multiple points in the field of view at up to 12,800 frames per second (fps), sufficient to characterize rapid fluid motion. Though our current system is capable of capturing images up to 120,000 fps, we limit our use here to 12,800 fps to reduce shot noise; reducing noise from various sources is an important part of the effort reported in this paper.

MATERIALS AND METHODS

Acoustic Nanoslit Fluidic Device. A straight-fingered unweighted interdigital electrode (IDT) was fabricated on a 500 μm thick, 127.68° *Y*-rotated *X*-propagating lithium niobate (LN) substrate with 20 finger pairs at a design frequency of 40 MHz. The specific design for the IDT fingers and layout is detailed in previous work.[20] Briefly, an open-circuit, 20-finger external reflector was used to prevent a bidirectional Rayleigh surface acoustic wave (SAW) from being generated from the IDT, instead producing a SAW propagating solely toward the nanoslit channel structure. The aperture of the IDT was 5 mm. The 40 MHz frequency was chosen as the lower limit for the generation of SAW in a 0.5 mm thick LN substrate;[34] lower frequencies will generate spurious Lamb or bulk waves. Higher frequencies reduce the wavelength of the propagating SAW, but neither the characteristics of the SAW nor its intrinsic effects on fluids exposed to the SAW are expected to change up to at least 250 MHz.[35] The attenuation length scales of the SAW in the substrate and the sound generated in the fluid are reduced as the frequency is increased from 40 to, for example, 250 MHz, but these length scales remain consistently much larger than the nanoscale thickness of our fluidic channel. The 40 MHz choice allows the SAW to travel the farthest when exposed to a fluid in the nanofluidic device with our 0.5 mm thick substrate. Because the interaction of a fluid trapped in a nanochannel is poorly understood at any acoustic frequency, we sought here to first focus on a choice most likely to generate a usefully interesting result via acoustogeometric streaming.[20]

A second 5 × 5 mm^2 LN wafer piece with the same crystal cut and thickness was then diced and etched on one side to produce a nanoscale indentation on its surface. The piece was bonded to the LN substrate with the IDT. The process is detailed in Zhang et al.[36] Briefly, the nanoscale indentation in the second LN wafer piece was produced by patterning a Cr sacrificial mask upon it, followed by reactive ion etching to form the 7 or 25 nm indentation for the devices for this study, and finally the removal of the Cr mask. Referring to Figure 1, a 600-μm diameter hole was drilled through the layer and into the nanoindentation to serve as a fluid inlet. After

https://doi.org/10.1021/acs.langmuir.4c04244
Langmuir 2025, 41, 5860−5869

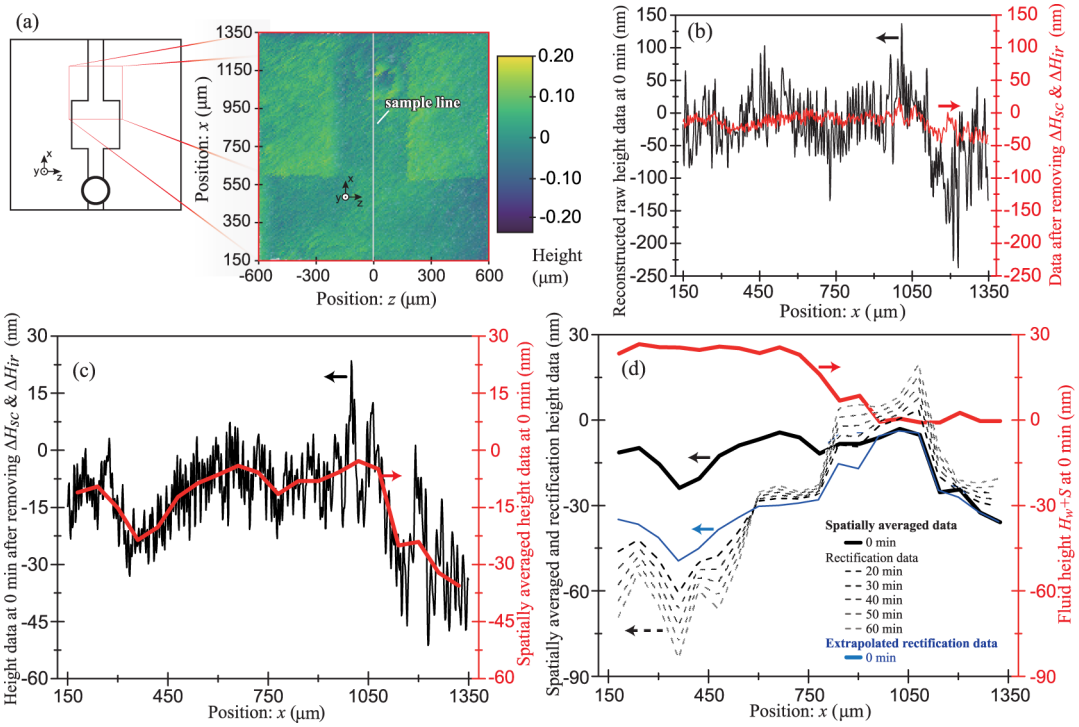

Figure 2. (a) The field of view (red box) is a portion of the fluidic nanoslit. Note that $(x,z) = (0,0)$ is at the center of the chip and the center of the enlarged channel region. A single frame of the reconstructed raw height data produced from the HSDHM measurement for the dry 25 nm channel device is shown, including all noise sources. The channel is visible as a darker colored region, though noise is prominent, especially around a scratch at $x = 1150$ μm, $z = 0$ μm. (b) The (black) raw reconstructed height is plotted along the SAW propagation x axis down the center of the channel ($z = 0$ μm), denoted as the sample line in (a). Removing the physical flaw-derived noise represented by $\Delta H_{sc} + \Delta H_{ir}$ produces (b, red) a less noisy result. Replotting this result (c, black) from −60 to 30 nm shows that there is still ample noise in the height data. By spatially averaging along -280 μm $\leq z \leq 280$ μm (staying within the fluid channel for all x values) and using a moving window average along x to reduce the total number of data points to 20, the noise (b, red) can be substantially reduced. However, there remain irregularities in the data, and (d, black), these irregularities are persistent over time. Fortunately, by using the (d, black dotted lines) rectification data—the displacement distribution measured with the dry channel for several minutes, as explained separately—the (d, red) final shot noise-limited result $H_w + S$ may then be found from a prediction of the (d, blue) creepage noise present at the time of the measurement, $t = 0$. The final result indicates the distribution of the fluid height in the channel along 20 points along the x axis ($z = 0$) as averaged for each point across the channel's width $-280 \leq z \leq 280$ μm.

piranha cleaning and oxygen plasma surface activation, the second LN piece was flipped and bonded at room temperature to the first LN piece. After the initial bond between the two LN pieces was formed, the device was heated in an oven to 300 °C to strengthen the bond. The basic structure of the nanoslit is shown in Figure 1b,c for the two nanoslit heights used in this study, 7 and 25 nm.

High-Speed Digital Transmission Holographic Microscopy. Our high-speed digital transmission holographic microscope (HSDHM; Lynceé-tec, Lausanne, Switzerland)[37] consisted of an illumination source (660 nm wavelength circular polarized laser), an interferometer specialized for HSDHM, a high-speed camera (NOVA S12, Photron, San Diego, CA, USA), and a data capture and control computer.[38] The system detects light passing through our device and fluid within the field of view. The length of the optical path varied as it passes through materials possessing different thicknesses and indices of refraction; for example, lithium niobate in the device and water in the nanoslit channel. The turnkey HSDHM system is designed to measure the phase shift of the transmitted light along its propagation direction at each camera pixel[39] with respect to reference light passed through the sample of interest. This produces a holographic data set that can be used to compute the height of the material in the sample if one knows the material's optical properties. When the light path passes through several materials, it becomes necessary to calculate the relative contribution of each material to the delay of the light as it passes through, all in comparison to the reference light. This effort makes it possible to resolve the structure of the device and the fluid within the field of view for each captured frame, in this case at up to 12,800 fps. Note that the field of view used in this experiment was either 2400 μm × 2400 μm for the 5× objective lens used with the 7 nm device, or 1200 μm × 1200 μm for the 10× objective lens used for the 25 nm device. Thus, the maximum fluid velocity we were able to resolve in this system was either 30.72 or 15.36 m/s, respectively; both velocities were much larger than the maximum fluid velocity we have observed in this and other studies, on the order of 1 m/s. Details of the HSDHM design,[40] including its optics,[38] imaging principles,[37] and noise reduction[41] are detailed in past publications.

Reconstruction and Postprocessing to Determine Fluid Height. The data from the HSDHM are in the form of a phase difference value, $\Delta\phi$, for each pixel measured across the entire field of view and for each frame over time. These data may be transformed to represent the total height, h, of the object measured at the pixel location through $h = n\Delta\phi$, where n is the index of refraction for the material. This assumes the material does not change along the path length, which is not the case in our system—nor many other systems of interest. This problem is typically solved by having a reference measurement in the field of view that represents a "zero" height. For example, one can imagine imaging a sessile droplet in the field of view; as long as one has a point located outside the bounds of the droplet in the field of view, then that can be defined as the zero height, and the droplet height can then be calculated from the phase shift relative to that point. The phase shift due to the substrate's presence is eliminated.

Another method—and our method of choice in this study—is to perform a set of measurements when the system is without the object of interest, in this case, the fluid in the nanoslit channel. We measured the dry LN device with no fluid in the channel to provide a reference

https://doi.org/10.1021/acs.langmuir.4c04244
Langmuir 2025, 41, 5860−5869

set of data. We define these measurements as the rectification measurements, rectifying the possible discrepancy that may arise from the presence of other objects not of interest along the measurement path, such as the LN pieces. Note that rectification measurements include both temporal and spatial components, and indeed, both will prove useful later in reducing the noise.

It is also necessary to deal with changes in the height that exceed one wavelength of the light over the field of view. Especially rapid changes in the height or the properties of the materials being measured can make it difficult to determine the correct height change. For example, a change in height of $m\lambda$, where m is a nonzero integer, produces no change in the phase of the light passing through the sample; such a change appears to be no change at all in our measurements without some form of correction. Our approach to phase unwrapping, the term given to the correction technique, is detailed elsewhere.[42] Essentially, we avoid the problem by restricting our measurement region to remain away from the edges of the nanoslit channel that might cause problems in height measurements,[43] so the thickness of the lithium niobate in the field of view is nearly constant, and we do not have rapid changes in the height of the fluid sample. The fluid in the channel may have a rapid change in height, but the channel itself is only 7 to 25 nm thick, much less than the wavelength of the light used.

The average index of refraction of LN is $n = 2.27$ at standard laboratory temperature ($T = 25$ °C) for a light wavelength of $\lambda = 660$ nm; LN is actually birefringent[44] though this does not affect our measurements due to the spatial averaging we use later on.[42] The index of refraction of deionized water used in our study was $n = 1.33$. While changes in temperature could lead to changes in the indices of refraction,[45] these changes will be less than 5% of the index of refraction at 0.01 for a 50 °C change,[46] in turn leading to an error an order of magnitude smaller than our eventual shot noise-limited error of $S = 1.248$ nm in the water height measurement. Therefore, we have reason to believe these effects will either be compensated for or will be negligible in our measurement. The effects of temperature changes of the lithium niobate on the measurement—whether due to thermal expansion or changes in the indices of refraction—are taken into account via rectification measurements. The temperature changes in the fluid cannot be handled this way, but because the volume of the fluid is minuscule (~17 μm^3 for the 7 nm device and ~45 μm^3 for the 25 nm device) and the distances over which heat would be transmitted are equally minuscule, the fluid's temperature is dominated by the temperature of the relatively enormous amount of lithium niobate that surrounds it.

Reconstruction of the fluid height data[38,40] for the fluid present in the nanoslit channel must also account for and mitigate errors from the measurement. There are several sources of noise in our HSDHM measurements. Physical flaws in the device are one source. Fortunately, because both pieces of LN are single crystals, there are no flaws within. However, there are surface scratches and surface irregularities on the LN. Creepage noise is another source, resulting from the long-term and nonuniform translation and distortion of the object in the field of view due to vibration and thermal expansion. There is also shot noise from the laser light source and the digital camera sensor.[38] Fortunately, each source of noise is easily identified, and the first step in reducing the noise is quantifying its components as follows:

$$H_w = H_{raw} - \Delta H_g - \Delta H_{creep} - S = H_{raw} - (\Delta H_{sc} + \Delta H_{ir}) - \Delta H_{creep} - S \quad (1)$$

where H_w is the actual height of the water in the channel, H_{raw} is the raw height data after phase unwrapping of the holographic data, ΔH_g is the general spatial optical noise from physical flaws including surface scratches (ΔH_{sc}) and irregularities (ΔH_{ir}), ΔH_{creep} is creepage noise, and, for our system, $S \approx 0.5$ nm is the shot noise. We next consider each source of noise, referring to Figure 2 as an example. Most of the data provided in this example are shown at the start of the fluid evaporation measurement, $t = 0$ min, and along the x-axis ($z = 0$).

We have observed in our setup that the surface scratches in the LN produce 20 to 30 pixel-sized regions of uniform ~100 nm amplitude changes in the prediction of the fluid height in the channel. This noise is represented by ΔH_{sc} and is temporally constant. The scratches that cause this noise are inevitable[47] and appear in all the measurements. The surface irregularities, ΔH_{ir}, produce larger, 40 to 60 pixel-sized spatially nonuniform ~100 nm amplitude changes in the prediction of the fluid height in the channel. Like the scratches, these are temporally constant and always appear. A roughly circular ring example of an irregularity can be seen in Figure 2a in the image at $x = 1150$ μm, $y = 0$ μm. This same irregularity appears as a peak and dip in the plot of the data along $z = 0$ in Figure 2b around $x = 1050$ μm. We eliminated these sources of noise by first employing threshold averaging[48] to eliminate changes in the data beyond a specified threshold; here the threshold was set at 100 nm and the dimensions of the regions were set as noted above. We then employed Gaussian nearest-neighbor averaging. The result is shown in red in Figure 2b.

Replotting this result in Figure 2c, black from −60 to 30 nm, shows that substantial high (spatial) frequency noise remains. Again, this is data at one time, $t = 0$ min, and only along $z = 0$. There are 800 distinct values for the fluid height along the x-axis in this data set. We have similar data sets parallel to the x-axis for other values of z. If we stay within the fluid channel, we have 373 sets of height data along x in the region of -280 μm$\leq z \leq 280$ μm. This data is not shown but is similar to those in Figure 2. Assuming that the fluid height does not significantly vary along the width of the channel, z, we next average the fluid height prediction along -280 μm$\leq z \leq 280$ μm for each value of x. In future work, we may seek to examine the data to determine whether we can reduce the amount of data averaged along z and try to identify variations in the fluid height along that direction. For now, we have only one prediction of the fluid height for each of the 800 values along the x-axis. To further reduce the noise, we used a moving window average along x to reduce the total number of data points from 800 to 20. The result is plotted in Figure 2c, red.

Even after this effort, however, there remain irregularities in the data, obvious in the replotted result in Figure 2d, black. The irregularities are also apparent in measurements of the dry channel: the rectification data in Figure 2d, dotted black, taken from $t = 20$ to 70 min. We waited for 20 min to start collecting rectification data because the complete evaporation of the fluid in the nanoslit channel in this example took about 10 min. Notice how the rectification data linearly changes in time and space. The rectification data have been processed in the same manner to produce the 20 data point set for each time as shown, and the creepage noise ΔH_{creep} in it is apparent. For example, notice the dip in the height data at about $x = 325$ μm: this dip consistently appears through all of the data. We may use this creepage noise data from the rectification measurement to eliminate it during the measurement by extrapolating back to the measurement time, $t = 0$ in this case, as shown in Figure 2d, blue, and by using that result to predict the distribution of the fluid height at that time. In other words, $H_{w,0\ min} + S = H_{raw} - (\Delta H_{sc} + \Delta H_{ir}) - \Delta H_{creep,\ 0\ min}$. This produces the final shot-noise-limited fluid height measurement $H_w + S$ shown in Figure 2d, red. This indicates the distribution of the fluid height in the channel along 20 points along the x-axis ($z = 0$). Notice that for values of $x < 750$ μm, the fluid height is about 25 nm, as one would expect, and for values of $x > 900$, the fluid height is about zero. The shot noise-limited error of the measurement is $S = 1.248$ nm in the water height measurement. In this example that illustrates the complex, multistep noise reduction method required to obtain the desired nanoscale fluid height data, the fluid meniscus is somewhere between $750 < x < 900$ μm.

Observation of Fluid Behavior: Evaporation at Slow Speeds or SAW-driven Flow at High Speeds. Deionized, ultrapure water was used in the nanoscale channels for these experiments. One calibrated pipette (Eppendorf, 0.1−2.5 μL) was used to introduce water into the device through the fluid inlet, as shown in Figure 1. The device was then quickly and carefully placed into the HSDHM with clean aluminum foil wrapped around the device in a closely

https://doi.org/10.1021/acs.langmuir.4c04244
Langmuir 2025, 41, 5860−5869

containing box with an open top to prevent air currents from the lab environment and the deposition of dust onto the device during the measurement. The experiment is illustrated in Figure 3. Holographic

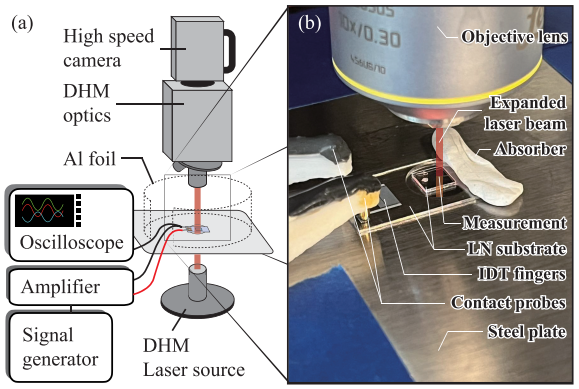

Figure 3. (a) HSDHM components (Lynceé-tec, https://www.lynceetec.com/highspeed-dhm/[38,40] in our turnkey system and (b) the device placement in the system. The 10× objective is shown; the 5 × objective was similar.

data was captured using the HSDHM after careful alignment to place the device's fluidic channel into the focal plane, using a 10× objective lens for the 25 nm device and a 5× objective lens for the 7 nm device. The objective lens power was selected on the basis of the dimensions of the nanoslit channel, ensuring most of it was captured in the field of view. Our system captured 1024× 1024 pixel frames at 12,800 fps for 0.156 s for each measurement, producing a data file approximately 4.77 GB in size.

RESULTS AND DISCUSSION

Observation of Slow Fluid Motion: Evaporation. We sought to observe the behavior of the fluid in the nanoslit channel over long time scales (>10 min) in both 25 and 7 nm height nanoslits. The nature of drying in nanoporous structures is a current topic of interest,[49,50] and viewing evaporation while the humidity of the local gas environment is not controlled is a particular challenge, especially for channels less than 40 nm in height. Moreover, in any intended applications of nanochannels driven by acoustofluidics or other methods, evaporation is always an important concern. Knowing its characteristics in comparison to the representative theory would be helpful.

We first examined the slow process of evaporation in the channels. The results for 25 and 7 nm nanoscale channels are shown in Figures 2 and 4. The raw data, including all noise, are provided in Figure 2. The evaporation of water observed via the HSDHM is presented as the processed results in Figure 4. The entire data capture process consisted of a series of 2000-frame holographic videos, each 0.156 s in length, captured every two min over t = 0,2,..., 8 min. Video for the rectification was captured at t = 20 min, long after the fluid completely evaporated from the channel. Complete evaporation took about 10 min in our system with both channels.

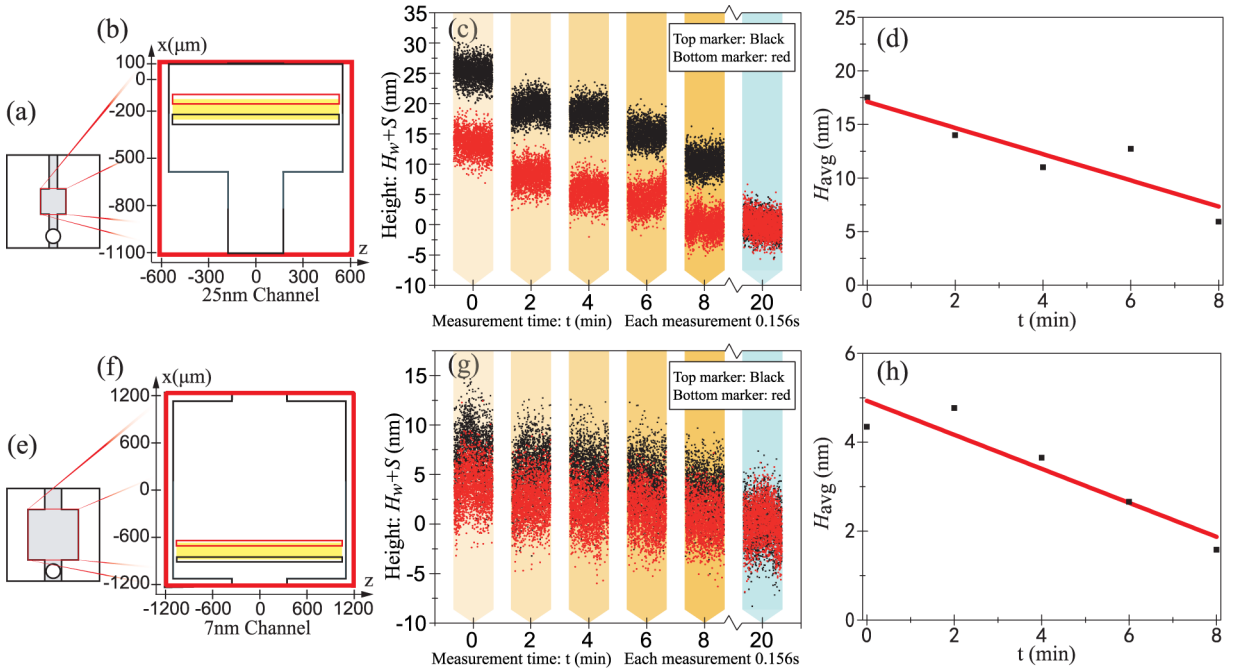

Figure 4. Evaporation-driven change in the fluid height within (a–d) 25 nm and (e–h) 7 nm nanoslits; the (a,e) fields of view for our HSDHM system are indicated, along with the (b,f) two fluid height measurement locations within the enlarged channel region. Note that (x,z) = (0,0) is always at the center of the chip and at the center of the enlarged channel region. For the 25 nm structure, (b) the fluid height measurement locations (red: x = −145 μm to −195 μm, and black: x = −245 μm to −295 μm) are illustrated where the HSDHM was used to produce (c) H_w + S, the fluid height after eliminating the various noise sources as detailed in Figure 2. These measurements were repeated 2000 times over a period of 0.156 s for each time t = 0,2,..., 8 min, where the fluid was mostly evaporated in both regions. Rectification data (blue background) was obtained at t = 20 min, showing the absence of the fluid in the channel as a fluid height of 0 nm. The height data for each time were spatiotemporally averaged and (d) plotted with respect to time, producing a linear decrease over time. Repeating this process for a (f,g,h) 7 nm nanoslit, we observed regions much closer to the bottom of the nanoslit chamber as indicated by the red (x = −675 μm to −725 μm) and black (x = −875 μm to −925 μm) regions.

https://doi.org/10.1021/acs.langmuir.4c04244
Langmuir 2025, 41, 5860−5869

For our 25 and 7 nm channels, we examined the evaporation of introduced water in the nanoslit channel over 8 min. Referring to Figure 4d,h, the evaporation of the water from the nanoslit channel reduced the fluid height linearly with respect to time in both the 25 and 7 nm channels. We defined two regions for data capture in each system, each region being 50 μm along the x-axis and 800 μm along the y-axis for the 25 nm nanoslit, and 1600 μm along the y-axis for the 7 nm nanoslit. The data were averaged over each of these regions. Because the fluid flow was principally in the x-axis direction, we chose two regions wide along y and narrow along x. We sought to avoid the edges of the nanoslit chamber to avoid their effect on the measurement result.[43] By comparing the results of these two regions, we could describe the movement of the fluid in the nanoslit as it evaporated. Initially, the entire nanoslit structure was filled with water. Over time, the water evaporated, progressively moving the meniscus from the top (large x) to the bottom (small x) in Figure 4. We started to collect data as the evaporation for the two regions became noticeable from the measurements.

The water height for the black region in Figure 4a started from around 25 nm (filled) and reduced to approximately 12 nm in Figure 4b; the water height in the red region started at around 14 nm and dropped to 0 nm. The fluid meniscus moved from the top (large x) to the bottom (small x). Averaged over the red and black regions—and including the small region between them (see the yellow region in Figure 4a)—the overall fluid height decreased as shown in Figure 4c. The overall fluid evaporation measured in this way appears to be linear; the average height decreased at a rate of $\frac{dH_{avg}}{dt} = -1.22 \pm 0.32$ nm/min.

We next sought to repeat this experiment, evaluating the evaporation from a 7 nm nanoslit channel (Figure 4d), approaching the practical limit of our method with our measurement equipment and process, and certainly the limit of our current fabrication method, with only one strike and passivation step to dry etch the lithium niobate.[36] The results are plotted in Figure 4(d–f), and the data were found to be substantially noisier, as expected. However, it was still possible to see that the water height in the black region started to decrease from around 7 nm (near full) to reach 4 nm after 8 min. The water height in the red region started at around 4 nm and decreased to about 0 nm. The evaporation appeared to be linear over the entire yellow region, with the average height of the fluid decreasing at a rate of $\frac{dH_{avg}}{dt} = -0.38 \pm 0.32$ nm/min.

It is important to note that the 0 nm height defined in Figure 4b,c,e,f was independently determined from the 12 min of rectification data, marked in blue at 20 min in Figure 4a,e. The fact that the fluid measurement data independently produced a final height of 0 nm was encouraging.

Comparing the two observed evaporation rates, we find the rate for the 7 nm channel to be 31% of that observed for the 25 nm channel. The cross-sectional area of the 7 nm tall, 570 μm wide channel was 4.0 μm^2, and the area of the 25 nm tall, 400 μm wide channel was 10 μm^2 (see Figure 1 for channel dimensions). Based on the 40% reduction of the cross-sectional area open to the atmosphere from the 25 nm device to the 7 nm device, it is reasonable to expect the 31% reduction in the evaporation rate. The fact that the reduction in the evaporation rate is less than the reduction in the channels' cross-sectional areas is likely due to the reduced mixing of air from the 7 nm channel with the air in the laboratory compared to the 25 nm channel; the relative humidity of the air in the thinner channel can remain higher.

Observed Evaporation Rates Compared to Theory. We may also compare these results to the expected rate of evaporation from the Hertz–Knudsen equation[51,52] if the continuum assumption is valid (see Supporting Information: the continuum assumption is indeed valid). With the knowledge that the vapor pressure for water is 2.3 kPa, our lab temperature is T = 25 °C, and the humidity in our laboratory is consistently 50%, the vapor pressure of water vapor in the air is (2.3 kPa)(50%) = 1.15 kPa. The heat of vaporization of water is 2257 kJ/kg; its gas constant is R = 461.5 J/(kg K), and its molecular mass is M = 18.02 g/mol. The mass flux in evaporation under these conditions, according to the Hertz-Knudsen equation, is as follows:

$$W = (P_s - P_v)\cdot\varepsilon_1\sqrt{\frac{M}{2\pi RT}} = 0.166\ \mathrm{kg\,m^{-2}\,s^{-1}} \quad (2)$$

where $\varepsilon_1 = 1$ is the evaporation coefficient.[51] The mass of the original droplet in these measurements was 10.5×10^{-8} g for the 25 nm tall nanoslit channel and 5.63×10^{-8} g for the 7 nm nanoslit. These suggest an evaporation time for the 25 and 7 nm cases of, respectively, 31.6 and 42.5 s based on the presumption that the fluid is completely exposed to the surrounding laboratory air. Both are approximately 15 times faster than the total evaporation time (around 10 min) observed in the nanoslit channels.

Knowing that there might be fluid loss during the brief time between when water is introduced into the channel and when the measurements begin, we sought to quantify the actual evaporation rate. Our basis for the comparison was the average speed, v_m, of the meniscus as the water within evaporates,

$$v_m = \frac{h_{avg}\cdot L_{ch}}{H_c} \quad (3)$$

where h_{avg} is the average height of the fluid present in the yellow region (see Figure 4a,d), L_{ch} is the width of the measured region, and H_c is the height of the channel. From the experimental data, the estimated speed of the fluid meniscus in the channels is 4.88 ± 1.28 μm/min in the 25 nm channel and 10.85 ± 2.29 μm/min in the 7 nm channel. This compares to a theoretical prediction from the Hertz-Knudsen eq 2 of 6.65×10^3 μm/min for the 25 nm channel and 4.73×10^3 μm/min for the 7 nm channel. Therefore, we speculate that the evaporation is initially rapid, decreasing significantly to a much lower equilibrium evaporation rate dependent upon the confined evaporation environment of the channel. Based on the prediction from the Hertz–Knudsen equation, the transient process is so short, almost instantaneous after the water filling, that most of our measurements could capture only the later equilibrium state.

The combination of a thin water layer and the high thermal conductivity of LN diminishes the impact of restricted heat transfer in our system. However, it is important to note that the LN itself does not generate heat, as the acoustic wave is generated; LN is not hysteretic.[53] Therefore, the only heat generated in this system is through viscous attenuation of the acoustic waves in the fluid. As mentioned before, however, we treated the system as an isothermal one because the volume and total heat capacity of the fluid are much less than these quantities for the surrounding LN.

https://doi.org/10.1021/acs.langmuir.4c04244
Langmuir 2025, 41, 5860–5869

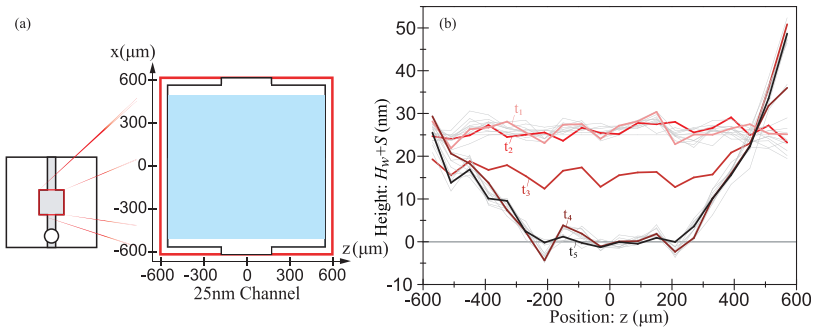

Figure 5. SAW-driven change in the fluid height within a 25 nm nanoslit. (a) FOV (red box) compared to the channel structure is marked at the left; calculation region marked as blue, with x range from −500 to 500 μm. (b) Relative water height H_w along the y-axis over time, with t_1 = 0.234 s, t_2 = 0.652 s, t_3 = 1.016 s, t_4 = 1.406 s, and t_5 = 1.797 s. The SAW propagates along the positive x axis. The gray curves were drawn every 1000 frames, while the red curves were drawn every 5000. Recall the frame rate of the camera was 12,800 fps.

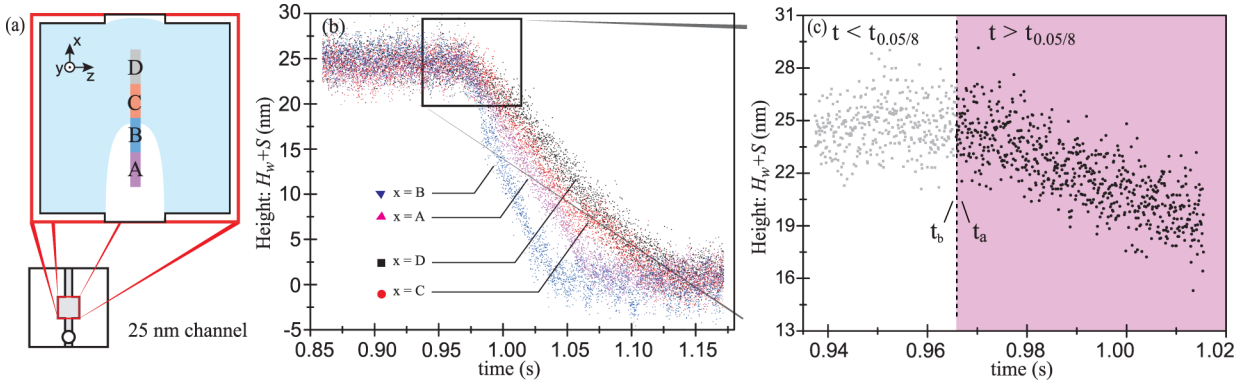

Figure 6. We examined (a) four (A,B,C,D) Δz = 60 μm × Δx = 200 μm regions, from x = −400 μm to x = 400 μm in the 25 nm channel device along the x axis as shown, seeking to measure (b) the height of the fluid in these regions. Data captured from the entire 1200 μm× 1200 μm region of the nanoslit chamber was used for noise reduction. A (c) closer look shows the scatter of the measured data, but which still contains sufficient information to estimate the onset of the fluid height's decrease over time through the use of the Student's t-test[59] (see text). The $t_{0.05/8}$ value is the 95% confidence value that a nine point group does not correspond to a known sample whose mean value is zero.

In this study, we considered the evaporation of a fluid meniscus from deep within a nanofluidic device and relatively far away from the open atmosphere, related to past studies of evaporation from nanofluidic devices.[54,55] Locally high humidity in deep and narrow fluidic channels slows the diffusion inside them, while the geometry of the nanoslit exit slows diffusion to the outside atmosphere, collectively impeding evaporation. As evaporation progresses, the humidity of the air present in the nanoslit gap will become much greater than the open atmosphere in the laboratory, thus reducing the rate of evaporation from the combined system. Xie et al.'s research demonstrated that using a high-speed dry nitrogen flow to maintain low humidity inside a nanoscale channel significantly accelerates evaporation,[49] highlighting the role of increased humidity in slowing evaporation. Furthermore, capillary trapping also contributes to reduced evaporation rates, a phenomenon more evident in smaller nanoslits where the channel height approaches the scale of a single water molecule, promoting capillary trapping under higher pressure conditions.[56] In contrast, larger channels typically exhibit this effect only under negative pressure.[57]

However, taking potential applications into consideration, it is actually helpful to have a slow evaporation rate due to nanoscale confinement. In an open environment, the evaporation of nanoscale fluid samples is widely known to be so fast as to make nanofluidics an unrealistic pursuit. In a nanoslit, however, such samples can remain intact for at least a few minutes, long enough for handling[36] and measurements to be completed.

Observation of Fast Fluid Behavior. We next consider the behavior of the fluid in the channel driven by SAW[58] over a very short time scale (1 ms) in the nanoslit. Rapid dewetting by SAW in a 150 nm nanoslit channel was previously reported[20] using standard high-speed optical microvideography. The technique used in that study fails for channels less than 50 nm in height. The fluid drainage from the nanoslit channel in that work is strongly dependent upon the lateral distribution of the SAW amplitude; typical IDT designs produce SAW with a laterally Gaussian distribution (i.e., along the z-axis direction in Figure 1). A fluid trapped in the nanoslit channel preferentially drains first along its centerline, along z = 0 as the SAW propagates along the x-axis. This dewetted region expands laterally along the z-axis direction at a slower rate while the fluid continues to flow along the x-axis away from the IDT, eventually draining all the fluid from the nanoslit channel.

Here, a channel of 25 nm height was examined using HSDHM, where the bright field and dark field fluorescent optical observation methods failed. The combined noise produced in the measurements prevented us from imaging the 7 nm height nanoslit channel system, indicating the limits of this measurement approach with current technology. We used the same process to fill the channel with water as was done for the evaporation experiment. The signal to drive the

https://doi.org/10.1021/acs.langmuir.4c04244
Langmuir 2025, 41, 5860−5869

SAW device was turned on 1 s after the HSDHM was started to ensure the dewetting process was captured. The main measurement consisted of one 25000-frame video at 12800 frames per second, followed by a rectification measurement of 2000 frames captured 20 min later, after the fluid had evaporated, to help once again reduce the measurement noise in postprocessing of the data.

We finally sought to evaluate this method to observe high-speed fluid flows in the 25 nm nanoslit channel, using SAW driven from an adjacent interdigital electrode at 39.7 MHz and a power of 781 mW (Figure 5), all in a manner similar to past devices with channel heights of over 100 nm.[20] Initially, the height of the fluid, H_w, was measured to be 25 nm everywhere along y; the nanoslit was full (t_1 = 0.234 s). The channel remained completely filled (t_2 = 0.652 s) until activation of the SAW at around 1 s, when the height decreased approximately 10 nm near the middle of the channel (t_3 = 1.016 s). Put another way, the fluid drainage was already underway at 0.016 s after starting the SAW. Near the edges, the fluid height did not decrease, consistent with past results showing the fluid being swept from the center due to the roughly Gaussian amplitude distribution of the propagating SAW.[20] The fluid height rapidly decreases to zero near the center of the channel at t = 1.09 s, where it remained dewetted while the SAW was left active (t_4 = 1.406 s and t_5 = 1.797 s). The spurious increase in the fluid height at x = 1200 μm is due to a small (∼1 nm) shift in the device position during measurement. We could have omitted or recaptured this data but instead chose to include it, noting again that the HSDHM is exquisitely sensitive to edges between disparate media.

By repeating this measurement at four positions along the SAW propagation direction—along the x-axis in Figure 6a—it becomes possible to estimate the speed of the dewetting. The four regions were defined in this way to ensure accurate capture of the particular time that dewetting started along the x-axis (z = 0). Figure 6b shows the average fluid height data for each region. Regions A and B—especially B—dewet most rapidly, while regions C and D dewet more slowly. As the fluid drains along the x-axis and from bottom to top in Figure 6a, it will be initially pinned at the corners of the inlet channel at the bottom, as illustrated with the light blue color representing the putative fluid configuration as it is drained from the nanoslit chamber through region B. This pinning will be released at some point as the fluid drains, which would cause a significant increase in the overall speed of the fluid's drainage from the chamber. We speculate that this is what is responsible for the increase in the speed of the fluid's height reduction to a maximum of 455 nm/s in region B before dropping to 172 nm/s as the fluid drains from region D.

In any case, the four regions appear to start dewetting at almost the same time. The exact time of dewetting for each region cannot be easily distinguished, principally due to the shot noise in the data coupled with the extraordinary speed of the fluid driven by acoustic forces. In order to produce a consistent estimate of the start of the dewetting for each region, we employed the Student's t-test[59] on two windowed subsamples, each composed of nine data points in time adjacent to a dividing line, as illustrated in Figure 6c. The window before the dividing line produced a t-test result, t_b, while the window after the dividing line (later in time) produced t_a. The start of dewetting was defined to be the time when one of the two selected windows produced a t-test result greater than the 95% confidence value of $t_{0.05/8}$ = 1.86. Table 1 indicates the time of the start of dewetting using this method for each of the four regions; the dewetting time for the four regions is likewise plotted in Figure 7.

Table 1. Student's t-Test to Identify the Onset of Dewetting in the Nanochannel: The Critical t Value of 95% Confidence is $t_{0.05/8}$ = 1.86[a]

Region	Time (s)	t_b	t_a
A	0.9655	0.35	2.75
B	0.9676	0.89	1.94
C	0.9681	1.69	1.89
D	0.9705	1.53	2.68

[a]The onset of dewetting is defined to be when either t_b or t_a exceeds this critical value

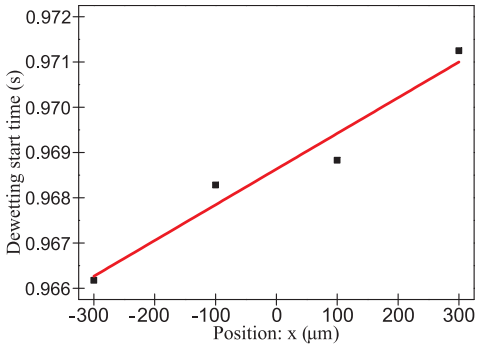

Figure 7. Start of dewetting plotted with respect to the center position along the x axis of each of the four regions in Figure 6a. The theoretical temporal error of all four points is 8 frames at 12800 fps: $t_{error} = 6.25 \times 10^{-4}$ s.

The data indicate a dewetting speed of $v_{sd} \approx 0.12$ m/s along the x-axis (see Figure 6a). Note that this is the average value of the meniscus' propagation speed with respect to the x-axis for each of the four regions: A, B, C, and D. Since we cannot use nanoparticles or dyes to characterize the flow at this small scale, the meniscus motion is useful in estimating the speed of the fluid flow due to acoustically generated forces. These results suggest that with proper arrangement of these measurement and calculation regions, it is possible to capture fluid meniscus movements when constrained to channels with a height of only 25 nm over a time scale of less than 1 ms. It also indicates that fluid transport of 12 cm/s is possible when driven by the SAW, a remarkable result.

CONCLUSIONS

In this article, an optical method of measuring nanofluidic flow with HSDHM is introduced, demonstrating the observation of fluid flows in nanochannels as small as 7 nm in height. Both long-term and high-speed measurements were shown at 25 nm, with evaporation measured in 25 and 7 nm channels and SAW-driven flow in 25 nm channels. These results appear to correlate with expectations, indicating a useful method for measuring fluid phenomena in nanofluidic devices. Evaporation was found to be much slower than theoretical predictions due to the enclosed channels that prevent rapid gas exchange with the laboratory environment. SAW-driven flow was found to occur at 12 cm/s, which is a remarkable result for fluid flow in such a small channel. Care must be exercised in identifying and reducing the impact of myriad sources of noise present in these measurements. Fortunately,

https://doi.org/10.1021/acs.langmuir.4c04244
Langmuir 2025, 41, 5860−5869

the spatiotemporal scales of the noise sources aided in their mitigation, save for the shot noise, which naturally defines the measurement floor in this optical measurement technique.

Due to the fact that the HSDHM distinguishes the fluid and the material of the nanoslit through the difference in indices of refraction, the measurement floor of this method also depends on the indices of refraction of both the fluid and the nanoslit material. With the combination of water and lithium niobate in our system, the shot-noise limit was approximately S = 1.248 nm in water height.

With the combination of rapid fluid flows that may be induced in these nanoscale channels with acoustic waves, alongside the slow pace of evaporation and past demonstrations of droplet manipulation and mixing at larger scales,[36] it may now be possible to devise devices for combining, splitting, mixing, and reacting various fluids at these small scales. As this measurement method is revised and improved, more information about how the acoustic wave actually drives discrete fluid samples in such devices should become available, enabling the design of single-cell and organelle-based testing protocols with acoustofluidics. Moreover, this tag-free method should facilitate a better understanding of fluid flows at the nanoscale by other means, as long as a change in fluid sufficient to produce an optically visible meniscus exists. The combination of speed and sensitivity via HSDHM may provide a unique window into the nanofluidics realm.

■ ASSOCIATED CONTENT

Supporting Information

The Supporting Information is available free of charge at https://pubs.acs.org/doi/10.1021/acs.langmuir.4c04244.

> Information on the continuity assumption for the fluid in the nanoslits; analysis of the statistical distribution of the noise identified in the HSDHM measurements; and calibration of the energy input into the SAW device (PDF)

■ AUTHOR INFORMATION

Corresponding Author

James Friend − *Medically Advanced Devices Laboratory, Department of Mechanical and Aerospace Engineering, University of California, San Diego, La Jolla, California 92093-0411, United States;* orcid.org/0000-0003-0416-2165; Email: jfriend@ucsd.edu

Authors

Siyang Yu − *Medically Advanced Devices Laboratory, Department of Mechanical and Aerospace Engineering, University of California, San Diego, La Jolla, California 92093-0411, United States*

Jeremy Orosco − *Medically Advanced Devices Laboratory, Department of Mechanical and Aerospace Engineering, University of California, San Diego, La Jolla, California 92093-0411, United States;* orcid.org/0000-0003-4433-5155

Complete contact information is available at: https://pubs.acs.org/10.1021/acs.langmuir.4c04244

Notes

The authors declare no competing financial interest.

■ ACKNOWLEDGMENTS

We are grateful to the Office of Naval Research, United States (grant 13423461), the National Science Foundation (grant ECCS 2314118), and the W. M. Keck Foundation, United States, for funding provided to JF in support of this work. We are also grateful to Yves Emery and the team at LynceéTec for assistance with adapting the HSDHM to this project's needs. Fabrication was performed in part at the San Diego Nanotechnology Infrastructure (SDNI) of UCSD, a member of the National Nanotechnology Coordinated Infrastructure, which is supported by the National Science Foundation (grant ECCS-1542148).

■ REFERENCES

(1) Chantipmanee, N.; Xu, Y. Nanofluidics for chemical and biological dynamics in solution at the single molecular level. *TrAC Trends In Anal. Chem.* **2023**, *158*, 116877.

(2) Rudyak, V.; Krasnolutskii, S.; Belkin, A.; Lezhnev, E. Molecular dynamics simulation of water-based nanofluids viscosity. *J. Therm. Anal. Calorim.* **2021**, *145*, 2983−2990.

(3) Habeeb, L. J.; Majdi, H. S. *Applications of Nanobiotechnology*; IntechOpen: London, United Kingdom, 2019.

(4) Di Trani, N.; Silvestri, A.; Bruno, G.; Geninatti, T.; Chua, C. Y. X.; Gilbert, A.; Rizzo, G.; Filgueira, C. S.; Demarchi, D.; Grattoni, A. Remotely controlled nanofluidic implantable platform for tunable drug delivery. *Lab Chip* **2019**, *19*, 2192−2204.

(5) Hahn, P.; Leibacher, I.; Baasch, T.; Dual, J. Numerical simulation of acoustofluidic manipulation by radiation forces and acoustic streaming for complex particles. *Lab Chip* **2015**, *15*, 4302−4313.

(6) Buongiorno, J. Convective transport in nanofluids. *J. Heat Trans.* **2006**, *128*, 240−250.

(7) Esfe, M. H.; Afrand, M. An updated review on the nanofluids characteristics: Preparation and measurement methods of nanofluids thermal conductivity. *J. Therm. Anal. Calorim.* **2019**, *138*, 4091−4101.

(8) Japar, W. M. A. A.; Sidik, N. A. C.; Saidur, R.; Asako, Y.; Nurul Akmal Yusof, S. A review of passive methods in microchannel heat sink application through advanced geometric structure and nanofluids: Current advancements and challenges. *Nanotechnol. Rev.* **2020**, *9*, 1192−1216.

(9) Tang, Y.-D.; Jin, T.; Flesch, R. C. Effect of mass transfer and diffusion of nanofluid on the thermal ablation of malignant cells during magnetic hyperthermia. *Appl. Math. Model.* **2020**, *83*, 122−135.

(10) Lin, L.; Chen, Q.; Sun, J. Micro/nanofluidics-enabled single-cell biochemical analysis. *TrAC Trends In Anal. Chem.* **2018**, *99*, 66−74.

(11) Rufo, J.; Zhang, P.; Zhong, R.; Lee, L. P.; Huang, T. J. A sound approach to advancing healthcare systems: the future of biomedical acoustics. *Nat. Commun.* **2022**, *13* (1), 3459.

(12) Ekinci, K. L.; Yakhot, V.; Rajauria, S.; Colosqui, C.; Karabacak, D. High-frequency nanofluidics: a universal formulation of the fluid dynamics of MEMS and NEMS. *Lab Chip* **2010**, *10*, 3013−3025.

(13) Connacher, W.; Zhang, N.; Huang, A.; Mei, J.; Zhang, S.; Gopesh, T.; Friend, J. Micro/nano acoustofluidics: materials, phenomena, design, devices, and applications. *Lab Chip* **2018**, *18*, 1952−1996.

(14) Kazoe, Y.; Kubori, S.; Morikawa, K.; Mawatari, K.; Kitamori, T. Characterization of pressure-driven water flows in nanofluidic channels by mass flowmetry. *Anal. Sci.* **2022**, *38*, 281−287.

(15) Tanaka, M.; Saeki, Y.; Hanasaki, I.; Kazoe, Y. Effect of finite spatial and temporal resolutions on super-resolution particle tracking velocimetry for pressure-driven flow in a nanochannel. *Microfluid. Nanofluid.* **2024**, *28* (6), 39.

(16) Robin, P.; Bocquet, L. Nanofluidics at the crossroads. *J. Chem. Phys.* **2023**, *158* (16), 160901.

(17) Emmerich, T.; Ronceray, N.; Agrawal, K. V.; Garaj, S.; Kumar, M.; Noy, A.; Radenovic, A. Nanofluidics. *Nat. Rev. Meth. Primers* **2024**, *4* (1), 69.
(18) Zhang, K.; Jia, N.; Li, S.; Liu, L. Rapid Determination of Interfacial Tensions in Nanopores: Experimental Nanofluidics and Theoretical Models. *Langmuir* **2019**, *35*, 8943−8949.
(19) Laser, D. J.; Santiago, J. G. A review of micropumps. *J. Micromech. Microeng.* **2004**, *14*, R35.
(20) Zhang, N.; Horesh, A.; Manor, O.; Friend, J. Powerful acoustogeometric streaming from dynamic geometric nonlinearity. *Phys. Rev. Lett.* **2021**, *126*, 164502.
(21) Kazoe, Y.; Shibata, K.; Kitamori, T. Super-Resolution Defocusing Nanoparticle Image Velocimetry Utilizing Spherical Aberration for Nanochannel Flows. *Anal. Chem.* **2021**, *93*, 13260−13267.
(22) Zhu, C.; Huang, K.; Siepser, N. P.; Baker, L. A. Scanning ion conductance microscopy. *Chem. Rev.* **2021**, *121*, 11726−11768.
(23) Thibault, P.; Elser, V. X-ray diffraction microscopy. *Annu. Rev. Condens. Matter Phys.* **2010**, *1*, 237−255.
(24) Lawrence, J.; Swerhone, G.; Leppard, G.; Araki, T.; Zhang, X.; West, M.; Hitchcock, A. Scanning transmission X-ray, laser scanning, and transmission electron microscopy mapping of the exopolymeric matrix of microbial biofilms. *Appl. Environ. Microbiol.* **2003**, *69*, 5543−5554.
(25) Prakash, K.; Diederich, B.; Heintzmann, R.; Schermelleh, L. Super-resolution microscopy: a brief history and new avenues. *Philos. Trans. R. Soc., A* **2022**, *380* (2220), 20210110.
(26) Yildiz, A.; Vale, R. D. Total Internal Reflection Fluorescence Microscopy. *Cold Spring Harbor Protoc.* **2015**, *2015*, 086348.
(27) Garcia-Sucerquia, J.; Xu, W.; Jericho, S. K.; Klages, P.; Jericho, M. H.; Kreuzer, H. J. Digital in-line holographic microscopy. *Appl. Opt.* **2006**, *45*, 836−850.
(28) Bishara, W.; Zhu, H.; Ozcan, A. Holographic opto-fluidic microscopy. *Optics Expr.* **2010**, *18*, 27499−27510.
(29) Merola, F.; Miccio, L.; Paturzo, M.; Finizio, A.; Grilli, S.; Ferraro, P. Driving and analysis of micro-objects by digital holographic microscope in microfluidics. *Opt. Lett.* **2011**, *36*, 3079−3081.
(30) Paturzo, M.; Finizio, A.; Memmolo, P.; Puglisi, R.; Balduzzi, D.; Galli, A.; Ferraro, P. Microscopy imaging and quantitative phase contrast mapping in turbid microfluidic channels by digital holography. *Lab Chip* **2012**, *12*, 3073−3076.
(31) Pandiyan, V. P.; John, R. Optofluidic bioimaging platform for quantitative phase imaging of LoC devices using digital holographic microscopy. *Appl. Opt.* **2016**, *55*, A54−A59.
(32) Luo, Y.; Yang, J.; Tu, X.; Huang, T.; Che, Z.; Song, C. Optofluidic phase-shifting digital holographic microscopy for quantitative measurement of microfluidic diffusion dynamics. *J. Appl. Phys.* **2020**, *127* (13), 134501.
(33) Yu, X.; Hong, J.; Liu, C.; Kim, M. K. Review of digital holographic microscopy for three-dimensional profiling and tracking. *Optical Engr.* **2014**, *53*, 112306−112306.
(34) Collignon, S.; Manor, O.; Friend, J. Improving and Predicting Fluid Atomization via Hysteresis-Free Thickness Vibration of Lithium Niobate. *Adv. Funct. Mater.* **2018**, *28* (8), 1704359.
(35) Dentry, M. B.; Yeo, L. Y.; Friend, J. R. Frequency effects on the scale and behavior of acoustic streaming. *Phys. Rev. E* **2014**, *89*, 013203.
(36) Zhang, N.; Horesh, A.; Friend, J. Manipulation and Mixing of 200 Femtoliter Droplets in Nanofluidic Channels Using MHz-Order Surface Acoustic Waves. *Adv. Sci.* **2021**, *8* (13), 2100408.
(37) Cuche, E.; Bevilacqua, F.; Depeursinge, C. Digital holography for quantitative phase-contrast imaging. *Opt. Lett.* **1999**, *24*, 291−293.
(38) Emery, Y.; Colomb, T.; Cuche, E. Metrology applications using off-axis digital holography microscopy. *J. Phys.: Photonics* **2021**, *3*, 034016.
(39) Kim, M. K. Principles and techniques of digital holographic microscopy. *SPIE Rev.* **2010**, *1*, 018005.
(40) Cuche, E.; Marquet, P.; Depeursinge, C. Simultaneous amplitude-contrast and quantitative phase-contrast microscopy by numerical reconstruction of Fresnel off-axis holograms. *Appl. Opt.* **1999**, *38*, 6994−7001.
(41) Charrière, F.; Colomb, T.; Montfort, F.; Cuche, E.; Marquet, P.; Depeursinge, C. Shot-noise influence on the reconstructed phase image signal-to-noise ratio in digital holographic microscopy. *Appl. Opt.* **2006**, *45*, 7667−7673.
(42) Zhang, S.; Orosco, J.; Friend, J. Onset of visible capillary waves from high-frequency acoustic excitation. *Langmuir* **2023**, *39*, 3699−3709.
(43) Vasan, A.; Orosco, J.; Magaram, U.; Duque, M.; Weiss, C.; Tufail, Y.; Chalasani, S. H.; Friend, J. Ultrasound mediated cellular deflection results in cellular depolarization. *Adv. Sci.* **2022**, *9* (2), 2101950.
(44) Warner, J.; Robertson, D.; Hulme, K. The temperature dependence of optical birefringence in lithium niobate. *Phys. Lett.* **1966**, *20*, 163−164.
(45) Schlarb, U.; Betzler, K. Refractive indices of lithium niobate as a function of temperature, wavelength, and composition: A generalized fit. *Phys. Rev. B* **1993**, *48*, 15613.
(46) Schiebener, P.; Straub, J.; Levelt Sengers, J.; Gallagher, J. Refractive index of water and steam as function of wavelength, temperature and density. *J. Phys. Chem. Ref. Data* **1990**, *19*, 677−717.
(47) Inevitable because handling these devices in the cleanroom during dicing and bonding inevitably produces a few scratches on even the most carefully handled samples.
(48) Frosio, I.; Kautz, J. Statistical Nearest Neighbors for Image Denoising. *IEEE Trans. Image Process.* **2019**, *28*, 723−738.
(49) Xie, Q.; Xiao, S.; Duan, C. Geometry-dependent drying in dead-end nanochannels. *Langmuir* **2017**, *33*, 8395−8403.
(50) Li, Y.; Chen, H.; Xiao, S.; Alibakhshi, M. A.; Lo, C.-W.; Lu, M.-C.; Duan, C. Ultrafast Diameter-Dependent Water Evaporation from Nanopores. *ACS Nano* **2019**, *13*, 3363−3372.
(51) Eames, I.; Marr, N.; Sabir, H. The evaporation coefficient of water: a review. *Int. J. Heat Mass Trans.* **1997**, *40*, 2963−2973.
(52) Lu, Z.; Kinefuchi, I.; Wilke, K. L.; Vaartstra, G.; Wang, E. N. A unified relationship for evaporation kinetics at low Mach numbers. *Nat. Commun.* **2019**, *10* (1), 2368.
(53) Kawamata, A.; Hosaka, H.; Morita, T. Non-hysteresis and perfect linear piezoelectric performance of a multilayered lithium niobate actuator. *Sens. Actuators, A* **2007**, *135*, 782−786.
(54) Li, Y.; Alibakhshi, M. A.; Zhao, Y.; Duan, C. Exploring ultimate water capillary evaporation in nanoscale conduits. *Nano Lett.* **2017**, *17*, 4813−4819.
(55) Ozsipahi, M.; Akkus, Y.; Beskok, A. Surface wettability effects on evaporating meniscus in nanochannels. *Int. Commun. Heat Mass Trans.* **2022**, *136*, 106166.
(56) Bao, B.; Qiu, J.; Liu, F.; Fan, Q.; Luo, W.; Zhao, S. Capillary trapping induced slow evaporation in nanochannels. *J. Pet. Sci. Engr.* **2021**, *196*, 108084.
(57) Duan, C.; Karnik, R.; Lu, M.-C.; Majumdar, A. Evaporation-induced cavitation in nanofluidic channels. *Proc. Natl. Acad. Sci. U. S. A.* **2012**, *109*, 3688−3693.
(58) Rufo, J.; Cai, F.; Friend, J.; Wiklund, M.; Huang, T. J. Acoustofluidics for biomedical applications. *Nat. Rev. Methods Primers* **2022**, *2* (1), 30.
(59) Student. The Probable Error of a Mean. *Biometrika* **1908**, *6*, 1−25.

https://doi.org/10.1021/acs.langmuir.4c04244
Langmuir 2025, 41, 5860−5869